Mimicking honeybee eyes with a 280° field of view catadioptric imaging system

2010 Bioinspir. Biomim. 5 036002

(http://iopscience.iop.org/1748-3190/5/3/036002)

Bioinsp. Biomim. **5** (2010) 036002 (13pp) doi:10.1088/1748-3182/5/3/036002

Mimicking honeybee eyes with a 280° field of view catadioptric imaging system

W Stürzl, N Boeddeker, L Dittmar and M Egelhaaf

Department of Neurobiology and Center of Excellence 'Cognitive Interaction Technology', Bielefeld University, Germany

E-mail: wolfgang.stuerzl@uni-bielefeld.de

Received 14 May 2010
Accepted for publication 13 July 2010
Published 6 August 2010
Online at stacks.iop.org/BB/5/036002

Abstract

We present a small single camera imaging system that provides a continuous 280° field of view (FOV) inspired by the large FOV of insect eyes. This is achieved by combining a curved reflective surface that is machined into acrylic glass with lenses covering the frontal field that otherwise would have been obstructed by the mirror. Based on the work of Seidl (1982 *PhD Thesis* Technische Hochschule Darmstadt), we describe an extension of the 'bee eye optics simulation' (BEOS) model by Giger (1996 *PhD Thesis* Australian National University) to the full FOV which enables us to remap camera images according to the spatial resolution of honeybee eyes. This model is also useful for simulating the visual input of a bee-like agent in a virtual environment. The imaging system in combination with our bee eye model can serve as a tool for assessing the visual world from a bee's perspective which is particularly helpful for experimental setups. It is also well suited for mobile robots, in particular on flying vehicles that need light-weight sensors.

(Some figures in this article are in colour only in the electronic version)

1. Introduction and motivation

Bees have remarkable navigation capabilities, e.g. they return reliably to a food source and to their hive in a complex and dynamic environment. To achieve this, they heavily rely on vision, as has been shown for path integration ('visual odometry') [3], beacon aiming [4], scene recognition [5] and visual guidance to a goal [6]. Since bees have tiny brains, they must have evolved efficient sensors and navigation strategies. Thus, technical systems, in particular small aerial vehicles with limited computing power, are also likely to profit from accurate understanding of the sensing, processing and navigation capabilities of these insects. Well-designed experiments are necessary to gain deeper insights into the various aspects of bee navigation capabilities. In order to test models of the observed behaviour it is advantageous to know the visual input the insects experienced during experiments. In the following, we present a small and light-weight imaging system consisting of a light-weight mirror-lens combination attached to a USB video camera that achieves a field of view (FOV) comparable to that of insect eyes. We also describe a model of the ommatidial lattice of the eyes of honeybees using the data reported in [1]. Compared to the previously published 'bee eye optics simulation' (BEOS) [2] that is limited to the frontal half of the viewing sphere (azimuth angles $|\alpha| \leqslant 90°$), our model takes the full FOV of the eyes into account. By using this model and remapping images captured with our imaging system according to the spatial resolution of honeybee eyes, we are able to get a glance at their visual perception of the world.

Our aim was to build a light-weight system that can be used as an intuitive tool for assessing the visual world from the bees' perspective by reconstructing their visual input. It may also serve as an insect-inspired vision system for mobile robots, especially for small flying vehicles.

1.1. Related work

To achieve a large FOV, panoramic imaging systems are commonly used that consist of a curved convex mirror in front of a camera lens (see [7] for an overview). By means of specifically designed mirror profiles, different desirable projections onto the image sensor can be achieved, e.g. [8–11]. There are a few publications, e.g. [12, 13], that also consider

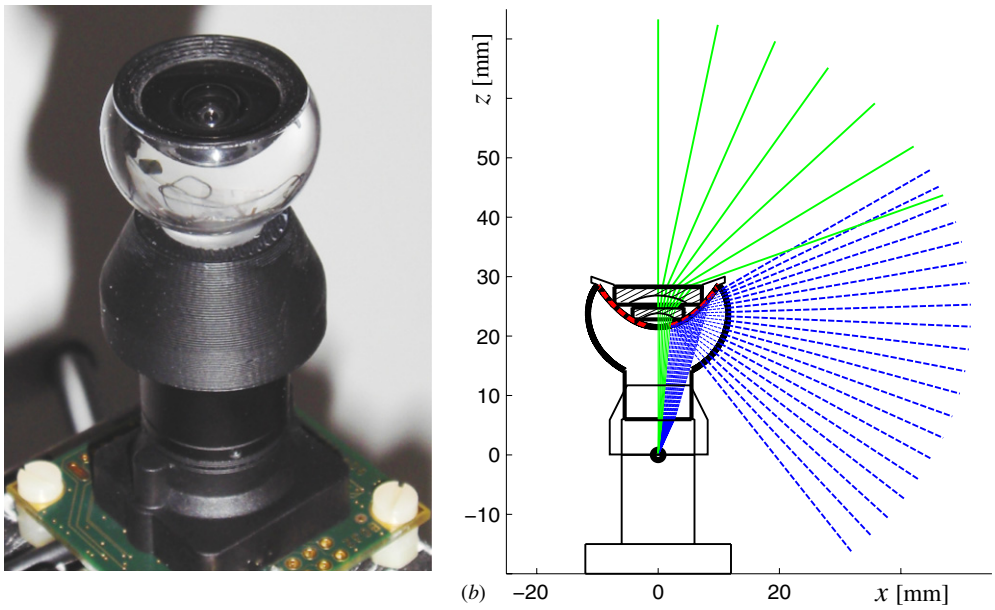

(*a*) (*b*)

Figure 1. (*a*) Photo of our 'bee eye' camera with 280° FOV. The diameter of the transparent globe is 23 mm. (*b*) Schematic drawing and raytracing diagram of the imaging system. Rays shown as dashed (blue) lines are reflected at a curved mirror surface (dashed red curve). Central rays (solid green lines) are refracted by two embedded lenses (hatched areas) before entering the acrylic glass through a circular area not covered by the reflective surface. The black dot indicates the nodal point of the camera lens. Since the imaging is symmetric with respect to the optical axis only rays for $x \geqslant 0$ are shown.

(This figure is in colour only in the electronic version)

the design of the refractive elements of such catadioptric systems[1]. However due to the obstruction caused by the mirror, such single-camera imaging systems do not cover the full FOV of most insect eyes. Multi-camera systems on the other hand, e.g. the Point Grey 'Ladybug' (see www.ptgrey.com), can provide large FOV and high-resolution images but lack close viewpoints which are important when imaging near objects, and are often too heavy for small unmanned aerial vehicles (UAVs)[2]. As described in the following section, our imaging system achieves a very large FOV of 280° and close viewpoints using a combination of reflective and refractive surfaces, a setup similar to, but considerably smaller than the one presented in [14]. Since we employ a standard RGB video camera for image capture that has no UV channel, it is not possible to accurately mimic colour vision in bees[3]. Recently, Chiao and colleagues developed colour filters that accurately match the spectral sensitivity of bee photoreceptors [16]. For capturing a single 'bee colour image' three images are taken with different colour filters selected using a filter wheel that was attached to a UV/Vis-sensitive CCD camera equipped with a 25 mm UV lens. Their setup is not well suited for recording in dynamic scenes and with higher frame rates. In addition, it does not capture wide FOV images. However, it might be possible to combine it with a panoramic imaging lens similar to that described in this paper, if care is taken regarding transmission and reflection of UV light. Researchers have also attempted to design artificial compound eyes by producing sophisticated lens arrays, see [17] for an overview. Even mircrofabrication of a spherical arrangement has been demonstrated [18]. However no image could be captured due to lack of curved sensor arrays. Recently, a joint European project entitled 'Curved Artificial Compound Eyes (CURVACE)', proposed to 'design, develop and assess artificial compound eyes, which will be composed of microlens arrays arranged on curved and flexible surfaces' (see www.curvace.net).

[1] A catadioptric optical system consists of refractive (dioptric) and reflective (catoptric) elements, i.e. they usually consist of a combination of lens(es) and mirror(s).

[2] The Point Grey 'Ladybug 3' (weight > 2 kg) consists of six cameras providing high-resolution panoramic images at a maximum frame rate of 15 Hz.

[3] Bees have three types of photoreceptors with maximum sensitivity at 340 nm (near UV), 450 nm (blue) and 540 nm (green) [15].

2. Description of the imaging system

To achieve the very large FOV of most insect eyes with a single camera we used a specifically designed catadioptric imaging system. A picture of the imaging system together with a raytracing diagram is shown in figure 1. The imaging system consists of two different optical paths: while the outer part of the camera image captures a scene via a convex reflective surface (dashed blue rays in figure 1(*b*)), the central part of the camera views the world through a combination of lenses (solid green rays in figure 1(*b*)). The imaging system captures a total FOV of approximately 280°, i.e. $\frac{1}{4\pi}\int_0^{\frac{1}{2}\mathrm{FOV}} 2\pi \sin\theta \,\mathrm{d}\theta = \frac{1}{2}(1-\cos 140^\circ) \approx 88\%$ of the viewing sphere.

The mirror lens combination is attached to a 3 mm S-Mount lens with manual iris control. Total weight (without camera) is approximately 40 g. Currently, we are using a USB board level camera (IDS μEye UI 1226LE, see www.ids-imaging.de) that provides frame rates up to 80 fps with a vertical resolution of 480 pixels.

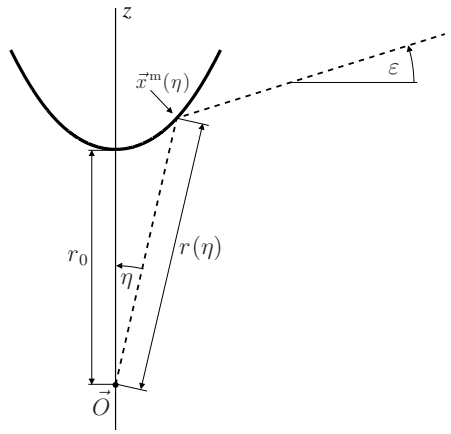

Figure 2. Illustration of the parameters defining the shape of a reflective surface with constant elevational gain. The thick curve depicts the mirror surface, and the dashed line shows a light ray reflected at this surface.

2.1. Shape of the reflective surface and acrylic glass body

For the mirror surface (dashed red curve in figure 1(*b*)) we used a shape with 'constant elevational gain' [8], described by

$$\vec{x}^{\,\mathrm{m}}(\eta,\alpha) = r(\eta)\vec{e}^{\,\mathrm{m}}(\eta,\alpha), \qquad \eta \in (0,\ \eta_{\max}), \tag{1}$$

$$r(\eta) = \frac{r_0}{\cos\left(\frac{a+1}{2}\eta\right)^{\frac{2}{a+1}}}, \tag{2}$$

$$\vec{e}^{\,\mathrm{m}}(\eta,\alpha) = (\sin\eta\cos\alpha,\ \sin\eta\sin\alpha,\ \cos\eta)^{\top}. \tag{3}$$

Figure 2 illustrates the parameters of equations (1)–(3). α is the azimuth angle defined in a plane orthogonal to the z-axis. Provided that the view point of the camera is at $\vec{O} = (0,0,0)^{\top}$, the geometry of this mirror leads to a linear mapping of η, the angle between the incoming rays and the optical axis, to elevation angle ε,

$$\varepsilon = a\eta - \frac{\pi}{2}, \tag{4}$$

where a is the 'elevational gain' of the reflective surface. The second parameter r_0 determines the distance to the apex. For our imaging system we used the parameter values $a = 7.5$, $r_0 = 25\,\mathrm{mm}$, $\eta_{\max} = 17.3^{\circ}$.

In order to avoid lateral occlusions by mechanical parts when mounting a mirror in front of a camera, the reflective surface defined by equation (1) was machined into a solid acrylic glass block and coated with a vapour-deposited aluminium layer. The outer acrylic glass surface is designed to be orthogonal to the incoming rays minimizing spurious reflections. As derived in [14], its shape is given by

$$\vec{x}^{\,\mathrm{p}}(\eta,\alpha) = \vec{x}^{\,\mathrm{m}} + [r(\eta_{\max}) - r(\eta)]\vec{e}^{\,\mathrm{m}}(\pi - a\eta,\alpha), \tag{5}$$

Due to the refraction at the planar acrylic glass surface facing the camera lens, the effective view point of the camera is about 3.5 mm further away from the reflective surface and the camera angle θ is reduced by a factor $1/n_{\mathrm{p}}$, i.e. $\eta = n_{\mathrm{p}}^{-1}\theta$, where $n_{\mathrm{p}} \approx 1.5$ is the refractive index of acrylic glass. See [14] for further details.

2.2. Embedded frontal lenses

In order to capture the part of the scene behind the reflective surface, i.e. in the viewing direction of the camera, an open area in the aluminium layer was produced by means of a small circular mask that covered the apex during vapour deposition, and two concave lenses were attached (see figure 1(*a*) and hatched areas in figure 1(*b*)). These embedded lenses cover a FOV of approximately 150° and thus provided sufficient overlap with the FOV of the reflective surface.

The black plastic fittings for the lenses were produced from CAD models using a 3D printer, as were the 8 mm long cylindrical element for mounting the acrylic glass body onto the camera lens (see figure 1(*a*)).

3. Combining the image parts

Both the central and the outer image part (see figures 4 and 5(*a*) and (*b*) for examples of camera images) were calibrated separately with Scaramuzza's Matlab 'OCamCalib' toolbox [19]. It is based on a very general mapping and distortion model that can also account for the strong distortions introduced by our catadioptric imaging system[4]. Calibration results are shown in figure 3. Both mappings from elevation ε to distance ρ from the image centre are almost linear.

Next, we describe how the transformation between the two coordinate systems was determined enabling us to remap the two image parts into a single continuous image.

3.1. Transformation between the reference frames of the two image parts

We estimated the rotation vector $\vec{w}^{\,\mathrm{ml}}$ and the translation vector $\vec{t}^{\,\mathrm{ml}}$ between the two reference frames by detecting corresponding corner points of a checkerboard pattern in the inner and outer part of several images (we used $N_p = 5$ images).

In the first step we determined the poses of the checkerboard in both coordinate systems for each image ($p = 1,\ 2,\ \ldots,\ N_p$). The rotation vectors $\vec{w}_p^{\,\mathrm{m}}$, $\vec{w}_p^{\,\mathrm{l}}$ and translations $\vec{t}_p^{\,\mathrm{m}}$, $\vec{t}_p^{\,\mathrm{l}}$ were estimated by minimizing the reprojection error of all corners visible in the two image parts (see figure 4),

$$\begin{aligned}
\left(\vec{w}_p^{\,\mathrm{m}}, \vec{t}_p^{\,\mathrm{m}}\right) &= \arg\min_{\vec{w},\vec{t}} \sum_{i\in V^{\mathrm{m}}} \left(\mathrm{proj}(\vec{X}_i(\vec{w},\vec{t})|\vec{c}^{\,\mathrm{m}}) - \vec{u}_{ip}^{\,\mathrm{m}}\right)^2, \\
\left(\vec{w}_p^{\,\mathrm{l}}, \vec{t}_p^{\,\mathrm{l}}\right) &= \arg\min_{\vec{w},\vec{t}} \sum_{i\in V^{\mathrm{l}}} \left(\mathrm{proj}(\vec{X}_i(\vec{w},\vec{t})|\vec{c}^{\,\mathrm{l}}) - \vec{u}_{ip}^{\,\mathrm{l}}\right)^2.
\end{aligned} \tag{6}$$

In equation (6), $\vec{X}_i(\vec{w},\vec{t}) = \underline{\underline{R}}(\vec{w})\vec{X}_i^0 + \vec{t}$ are the 3D positions of the corner points on the observed patterns. Here we have defined $\vec{X}_i^0 = (x_i,\ y_i,\ 0)^{\top}$ to be the 3D coordinates of the corner points when the checkerboard is aligned with the respective coordinate system, and $\underline{\underline{R}}(\vec{w})$ is the rotation matrix that is linked to rotation vector $\vec{w}$ via Rodrigues'

[4] The appropriateness of the calibration model for describing the mapping of our imaging system can also be inferred from the low reprojection error reported by the toolbox which was, on average, 0.3 pixels for both image parts.

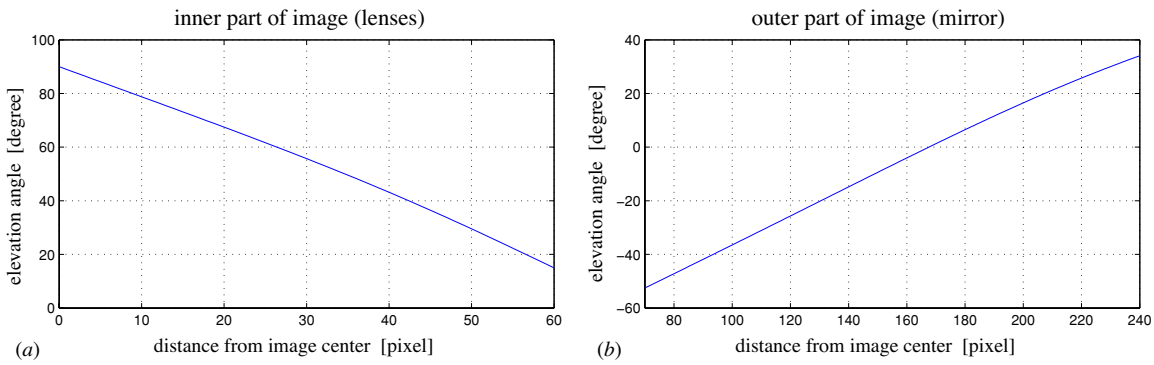

Figure 3. Mapping of the radial distance from the image centre to the elevation angle, as determined by calibration. (*a*) Angular mapping for the central image part, i.e. for imaging through the frontal lenses. (*b*) Angular mapping for the outer image part, i.e. for imaging via the reflective surface.

Figure 4. Example of a camera image used for estimating the translation $\vec{t}^{\,\mathrm{ml}}$ and rotation $\vec{w}^{\,\mathrm{ml}}$ between the reference frames of the inner and outer image part (see text for details). Corner points in both image parts corresponding to the same point on the pattern are connected by dashed lines. The dashed circle marks the boundary between the inner and outer image part.

rotation formula [20]. $\vec{u}^{\,\mathrm{m}}_{ip}$ and $\vec{u}^{\,\mathrm{l}}_{ip}$ are the corresponding image coordinates of corner points in the outer part (the mirror part) respectively inner part (the lens part) of the camera image. V^{m}, V^{l} describe the sets of indices of corner points visible in the two image parts and $\vec{c}^{\,\mathrm{m}}$ and $\vec{c}^{\,\mathrm{l}}$ contain the intrinsic calibration parameters.

In the second step, we then minimized

$$\sum_{p=1}^{N_p}\sum_{i}\left(\underline{\underline{R}}(\vec{w}^{\,\mathrm{ml}})\left(\underline{\underline{R}}(\vec{w}^{\,\mathrm{l}}_p)\vec{X}^0_i+\vec{t}^{\,\mathrm{l}}_p\right)+\vec{t}^{\,\mathrm{ml}}-\left(\underline{\underline{R}}(\vec{w}^{\,\mathrm{m}}_p)\vec{X}^0_i+\vec{t}^{\,\mathrm{m}}_p\right)\right)^2 \tag{7}$$

with respect to $\vec{w}^{\,\mathrm{ml}}$ and $\vec{t}^{\,\mathrm{ml}}$. The relative rotation of the coordinate systems was estimated to be very small: the rotation vector is $\vec{w}^{\,\mathrm{ml}} \approx (0.005, 0.014, 0.001)^{\top}$, its length approximately 0.015, corresponding to a rotation angle of about 0.85°. The translation vector is $\vec{t}^{\,\mathrm{ml}} \approx (-0.38\,\mathrm{mm}, -1.07\,\mathrm{mm}, 3.36\,\mathrm{mm})^{\top}$ and viewpoints lie only about $\|\vec{t}^{\,\mathrm{ml}}\| \approx 3.5$ mm apart. Thus with the exception of very close objects (closer than about 10 cm)[5], we can treat the whole system as a single-viewpoint system and remap the two image parts to a single continuous image of 280° FOV.

3.2. Image remapping and stitching

For producing a single continuous image, both image parts are first remapped to images I^{l} and I^{m} with radial resolution of 1°/pixel, using bilinear pixel interpolation. For this, look-up tables were calculated from the calibration results and the estimated relative orientation $\vec{w}^{\,\mathrm{ml}}$. Since camera images have significantly lower angular resolution in the central part (approx. 1.5°/pixel) than in the outer part (approx. 0.5°/pixel), we compensate for this by blurring the outer part with a Gaussian before combining the image parts.

Finally, we apply linear blending to obtain a single continuous image (called 'combined image' in the following), $I^{\mathrm{c}}(u,v) = b(u,v)I^{\mathrm{l}}(u,v) + (1-b(u,v))I^{\mathrm{m}}(u,v)$. Since the remapped images $I^{\mathrm{l}}(u,v)$ and $I^{\mathrm{m}}(u,v)$ overlap in an annular region of about 5 pixels width, we use a blending length of 5 pixels in which $b(u,v)$ changes radially between 0 and 1. Examples of camera images and the resulting combined images with continuous 280° FOV are shown in figure 5. The large FOV is illustrated in figure 6 where we have remapped the combined image of figure 5(*c*) onto a sphere.

Our current implementation of the described image remapping and stitching operation (whose complexity scales linearly with number of pixels) takes about 10 ms per frame (C program running on a laptop with Mobile Core 2 Duo T7500 CPU). Thus, online processing of images running at 25 fps should be achievable even on UAVs with less onboard computing power.

[5] The effect of a non-single viewpoint also depends on the angular resolution of the imaging system. The difference in the elevation angle for an object at distance r and angle ε can be estimated by $\Delta\varepsilon \approx \frac{d}{r}\cos\varepsilon$, where d is the distance between viewpoints. Thus for an angular resolution of about 1.5°/pixel (as in the inner part of the camera image) and $d = \|\vec{t}^{\,\mathrm{ml}}\| \approx 3.5$ mm the minimum distance that causes a shift smaller than one pixel is approximately $r_{\min} \approx \frac{3.5\,\mathrm{mm}}{1.5\pi/180}\cos 30° \approx 116$ mm at $\varepsilon = 30°$ (the elevation angle where the two image parts overlap). For the 'bee's view' presented in section 4 the angular resolution of ommatidia is lower than 2.5° and thus $r_{\min}$ is reduced to about 69 mm.

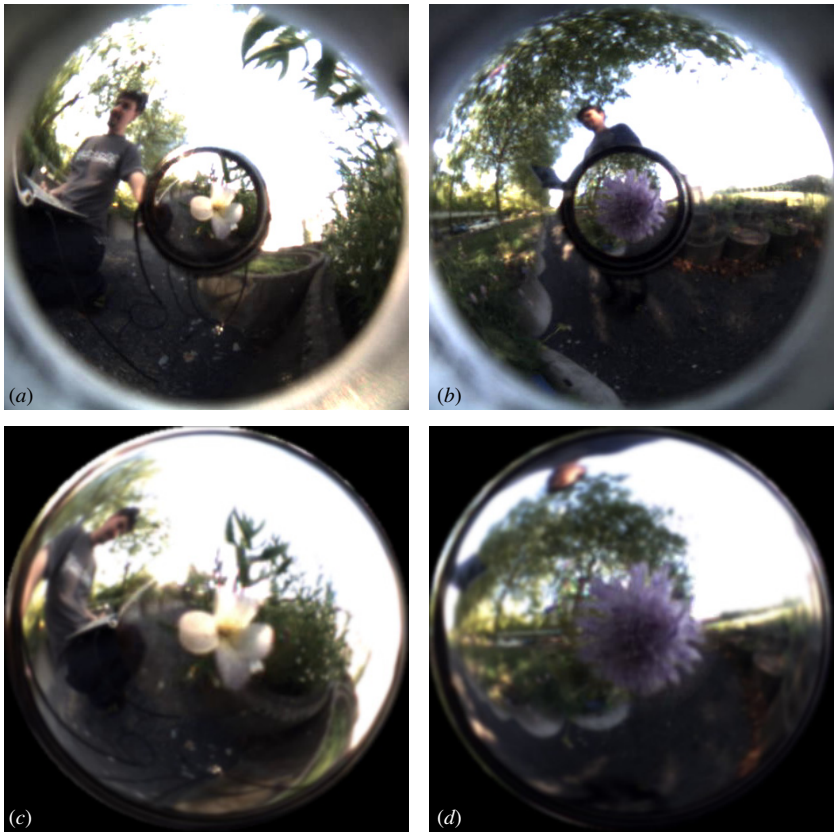

Figure 5. (*a*), (*b*) Camera images (460 × 460 pixels) extracted from a Motion JPEG movie recorded at 75 fps. (*c*), (*d*) Combined images with continuous 280° FOV (300 × 300 pixels) created from the images shown in (*a*) and (*b*).

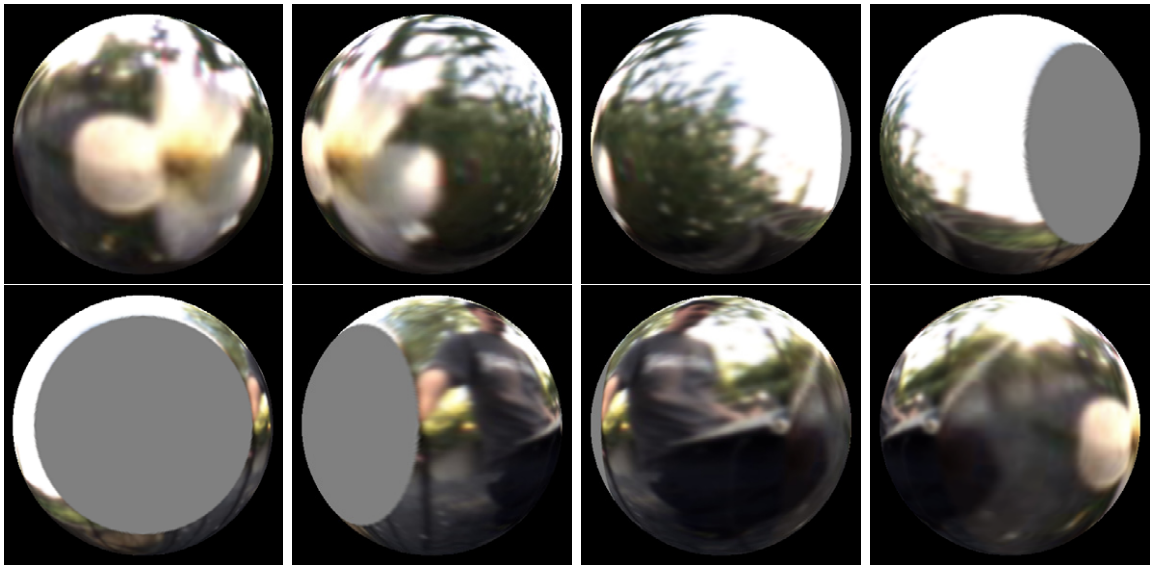

Figure 6. Combined image of figure 5(*c*) mapped to a sphere, shown for different viewing directions in 45° steps.

4. Creating a bee's view

In the following sections, we describe how the combined images of 280° FOV can be mapped to a simulated compound eye mimicking the spatial resolution of honeybees.

With respect to spatial resolution, a compound eye is usually described by two parameters, the interommatidial angle and the acceptance angle [21]. The values of these angles generally change with position on the insect eye.

4.1. Interommatidial angles and viewing directions

Seidl [1] measured interommatidial angles, i.e. the angular spacing between neighbouring ommatidia, over the full FOV

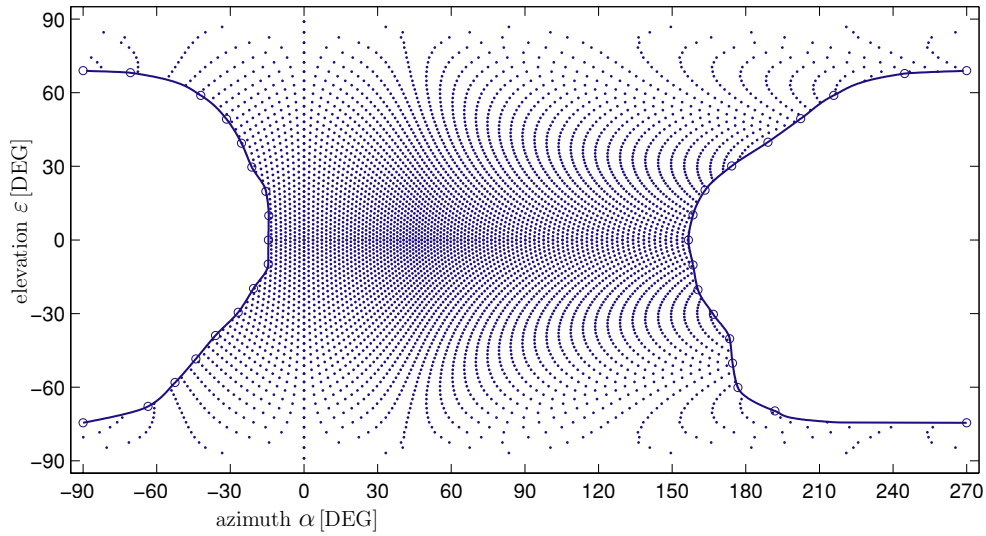

Figure 7. Viewing directions of ommatidia computed by the model for the left eye. The continuous curves demarcate the part of the sphere not visible to the eyes of a worker bee. This area is not symmetric with respect to the equator.

of a worker bee's eyes by rotating a microscope around the head while illuminating the eyes from inside ('antidromic illumination'). Based on Seidl's work, Giger [2] found a simple approximative description of azimuth and elevation angles of the ommatidia in the frontal hemisphere that accounts for the measured interommatidial angles. Giger's model whose computer implementation was called 'BEOS' is based on the observation that the horizontal interommatidial angles are quite constant along the vertical and that the vertical interommatidial angles predominantly depend on elevation. He also observed an approximately horizontal symmetry (with respect to the equator) of the ommatidial lattice, in addition to the obvious vertical symmetry between the two eyes. The resulting model of viewing directions is restricted to the frontal hemisphere (azimuth angle $|\alpha| \leqslant 90°$) and also ignores the binocular overlap of left and right FOV, i.e. the part of each eye viewing the contralateral side is not represented. In the following, we extend Giger's model to the full FOV of a bee's eyes based on the measurements published in [1]. This also includes the binocular zone of the eyes but ignores the separation between the eyes.

Motivated by Giger's model [2] and Seidl's measurements [22], we decided to split each eye into four zones, defined by the azimuth angle $-90° \leqslant \alpha \leqslant 0°$ and $0° \leqslant \alpha \leqslant 270°$ and the elevation $\varepsilon \leqslant 0$ and $\varepsilon \geqslant 0$, respectively. For each zone, the model produces a one-dimensional array of elevation angles ε_j^z and a two-dimensional array of azimuth angles α_{ij}^z ($z = 1, 2, 3, 4$). Please note that this coordinate system is rotated by 90° with respect to coordinate system of the imaging system (see section 2), i.e. the z-axis of the imaging system is oriented along the x-axis of the bee eye coordinate system (elevation angle $\varepsilon = 0°$ and azimuth angle $\alpha = 0°$). The rules determining the viewing directions of the model eye are given in the appendix. The parameters of the model were adjusted so that the spatially varying interommatidial angles and the total number of ommatidia are in the range reported by Seidl [1]. The model varies the horizontal interommatidial angle between 2.4° and 4.6° and the vertical interommatidial angle between 1.5° and 4.5°. The highest horizontal resolution (the smallest horizontal interommatidial angle) is between $\alpha = 30°$ and $\alpha = 45°$ (where the vertical midline of the head defines the azimuth angle $\alpha = 0°$). The highest vertical resolution is at the equator of the eye, corresponding to elevation angle $\varepsilon = 0°$, and decreases towards the dorsal and ventral rim of the eyes.

For determining the border of the visual field, the measurements of Seidl were incorporated and interpolated where necessary (see the continuous curves in figure 7 and the appendix). Only a small region where the thorax is located is not covered by the eyes of a bee [22]. This 'dead space' has its maximum horizontal extent of 47° at the equator ($\varepsilon = 0°$), and its maximum vertical extent from $\varepsilon_{\min} = -65°$ to $\varepsilon_{\max} = 35°$ at azimuth angle $\alpha = \pm 180°$ [1]. The total number of ommatidia per eye produced by the model is 5453, close to the numbers reported by Seidl. He counted ommatidia of seven eyes and their numbers ranged from 5261 to 5498 with median value of 5450.

The resulting directions for the left eye are shown in figure 7 in an equi-rectangular projection. Due to distortions introduced by the projection, distances between ommatidia appear larger for higher elevations than they are on the unit sphere using the mapping $(x_{ij}, y_{ij}, z_{ij}) = (\cos\alpha_{ij}\cos\varepsilon_j, \sin\alpha_{ij}\cos\varepsilon_j, \sin\varepsilon_j)$, see figure 8. The viewing directions of the right eye can be obtained by simply replacing azimuth angle α with $-\alpha$. In figure 9, viewing directions of both eyes are shown in a single diagram. The dashed curves circumscribe the area not covered by our 'bee eye' camera which mostly overlaps with the part on the viewing sphere not visible to the bee's eyes.

4.2. Acceptance angles

Each ommatidium receives light from within its visual field. The angular sensitivity of a photoreceptor is usually described

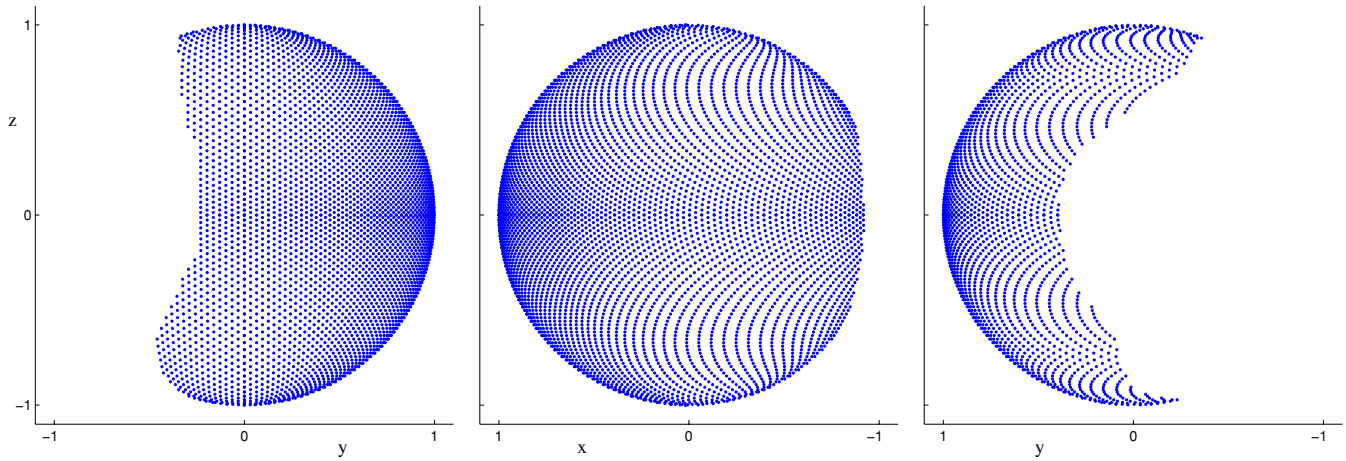

Figure 8. Viewing directions of the model illustrated on the unit sphere. For better visibility this is shown for three different ranges of the azimuth angle α (from left to right): $-90^\circ \leqslant \alpha \leqslant 90^\circ$, $0^\circ \leqslant \alpha \leqslant 180^\circ$ and $90^\circ \leqslant \alpha \leqslant 270^\circ$.

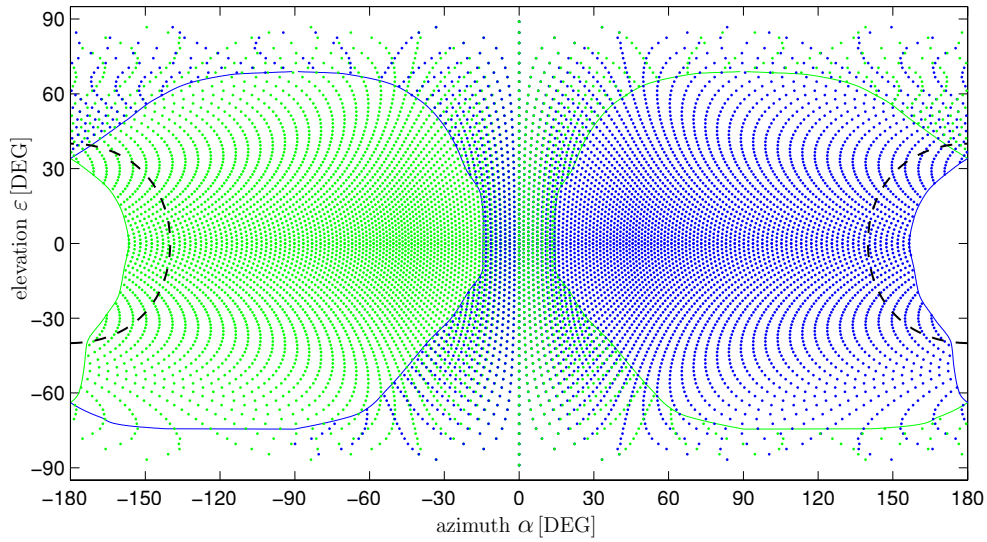

Figure 9. Viewing directions of ommatidia of both eyes. The dashed curves encircle the area not covered by the 280° of the imaging system. The continuous curves depict the limits of the visual fields for each eye. Note that some of the viewing directions of the left and the right eye coincide in the frontal FOV because the model produces symmetrical directions in this part of the eye.

by a two-dimensional radially symmetric Gaussian function [2, 21]. Its full width at half maximum (FWHM) is called 'acceptance angle' $\Delta\rho$.[6] In order to achieve optimal coverage of the visual field, the acceptance angle should be adjusted to the local interommatidial angles, i.e. there should be neither undersampling (acceptance angle too small) nor oversampling (acceptance angle too large with respect to the interommatidial angle). Since interommatidial angles change with position on the bee's eye, similar variations can be expected for the acceptance angle as well.

However, there are only a few direct, i.e. electrophysiological measurements of the acceptance angle of bee photoreceptors. For the frontal part of the eye (azimuth angle $\alpha \approx 0^\circ$, elevation angle $\varepsilon \approx 0^\circ$), i.e. in a region where interommatidial angles are comparatively small, Laughlin and Horridge [23] measured an acceptance angle of 2.6° that is in very good agreement with 2.6° reported in [24]. In addition, for the specialized dorsal rim area whose UV photoreceptors show high polarization sensitivity, Labhart [24] found two different types of photoreceptors that had either narrow but still larger receptive fields than in the frontal part of the eye, $\Delta\rho \approx 3.2^\circ$ or wide receptive fields, $\Delta\rho \approx 5.5^\circ$. However, since these measurements were done in the specialized rim area, it is not clear whether theses results can be generalized to other regions in the eye.

It is worth noting that the acceptance angle cannot be inferred from the diffraction limit of the facet lens, $\Delta\rho_{\text{diff}} = \lambda/D$, where λ is the wavelength and D is the diameter of the facet. The diffraction limit calculated from the lens diameter is, at least for the frontal part of the eye, considerably smaller than the measured acceptance angle [25]. For $D \approx 20\,\mu$m and $\lambda = 550$ nm we find $\Delta\rho_{\text{diff}} = 0.0275$ rad $\approx 1.6^\circ$, compared

[6] The FWHM $\Delta\rho$ is linked to the standard deviation σ of a Gaussian according to $\Delta\rho = \sqrt{8\ln 2}\,\sigma \approx 2.35\,\sigma$.

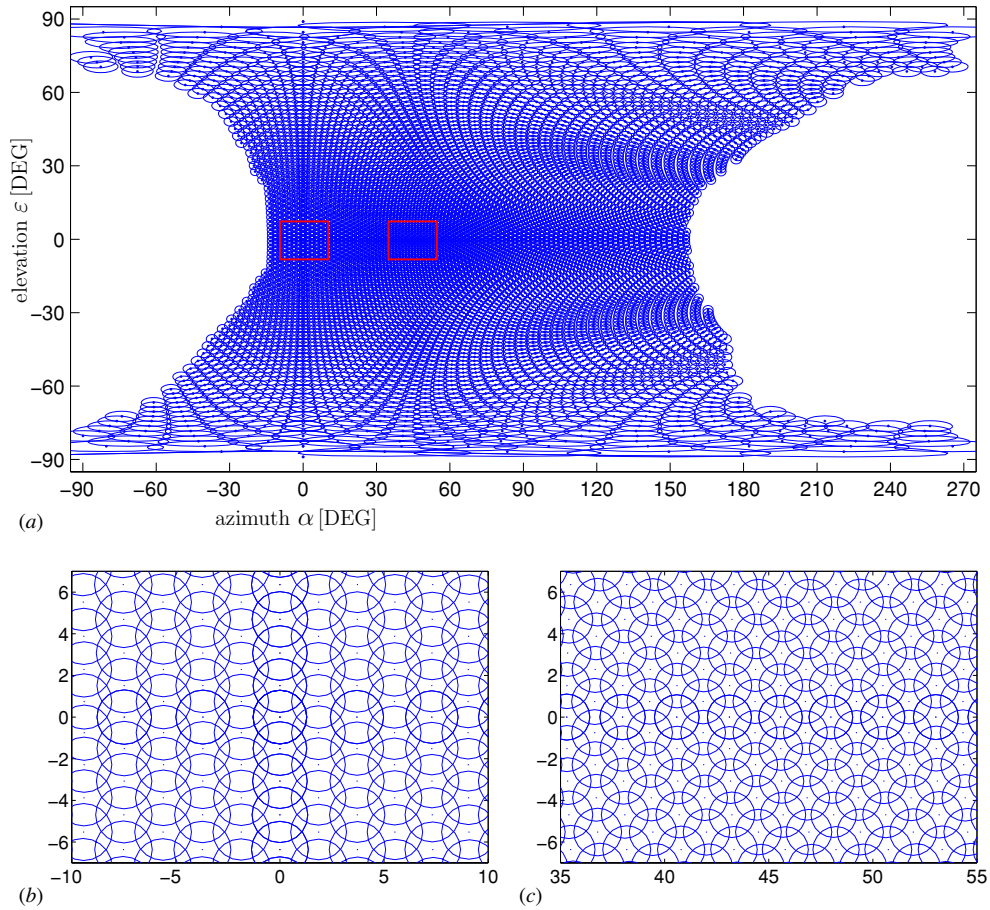

Figure 10. (*a*) Viewing directions and receptive fields of ommatidia as computed by the model. The ellipses show equi-rectangular projections of circles on the sphere with diameter equal to the acceptance angle. The rectangles highlight areas that are displayed magnified below: (*b*) frontal region with interommatidial angles $\Delta\varphi_h \approx 3.7^\circ$, $\Delta\varphi_v \approx 1.5^\circ$ and acceptance angle $\Delta\rho \approx 2.6^\circ$ as reported in [23, 24]; (*c*) central region of the eye (azimuth $\alpha \approx 45^\circ$) with minimum interommatidial angles $\Delta\varphi_h \approx 2.4^\circ$, $\Delta\varphi_v \approx 1.5^\circ$ as well as the minimum acceptance angle $\Delta\rho \approx 2.1^\circ$.

to the measured value $\Delta\rho \approx 2.6^\circ$. Nevertheless, the lens diameter changes over the eye in a similar way as one would expect for a diffraction limited eye with the acceptance angle adjusted to the local interommatidial angles: the lens diameter is largest and thus $\Delta\rho_{\text{diff}}$ is smallest in the central part of the eye where the interommatidial angles are small, and the lens diameter decreases ($\Delta\rho_{\text{diff}}$ increases) towards the periphery of the eye with larger interommatidial angles. According to the measurements of Seidl [1], lens diameters of facets vary from about 17 μm in the dorsal area to approximately 24 μm in the central area of the eye.

In summary, it is still unclear how acceptance angles are distributed over the whole visual field but there are some indications that the acceptance angle changes with interommatidial angles. Therefore, and in contrast to the BEOS model [2] that uses a constant acceptance angle of 2.6°, we decided to estimate the local acceptance angle in dependence of both vertical and horizontal local interommatidial angles according to

$$\Delta\rho(\alpha,\varepsilon) = 1.1\sqrt{\Delta\varphi_v(\alpha,\varepsilon)\Delta\varphi_h(\alpha,\varepsilon)} \approx \sqrt{1.7\Delta\varphi_v(\alpha,\varepsilon)\cdot 0.7\Delta\varphi_h(\alpha,\varepsilon)}. \quad (8)$$

Hence the acceptance angle is chosen to be proportional to the geometric mean of the vertical and horizontal local interommatidial angle. For our model we have in the frontal part $\Delta\varphi_v(\alpha \approx 0^\circ, \varepsilon \approx 0^\circ) \approx 1.5^\circ$ and $\Delta\varphi_h(0^\circ, 0^\circ) \approx 3.7^\circ$, resulting in $\Delta\rho(0^\circ, 0^\circ) \approx 2.6^\circ \approx 1.7\Delta\varphi_v(0^\circ, 0^\circ) \approx 0.7\Delta\varphi_h(0^\circ, 0^\circ)$ in agreement with the electrophysiological measurements [23, 24]. In the dorsal rim area, i.e. close to $\varepsilon \approx 90^\circ$, where our model uses $\Delta\varphi_h \approx 3.7$ and $\Delta\varphi_v \approx 4.5^\circ$, it estimates the acceptance angle to be $\Delta\rho \approx 4.5^\circ$ which is in the range of the values reported by Labhart [24]. Figure 10 shows the result of the full bee eye model, i.e. viewing directions of ommatidia and their angular sensitivity.

4.3. Remapping of the combined image according to the bee eye model

In order to implement the Gaussian shaped acceptance function, we used 9×9 sampling directions per ommatidium and computed weighted averages. The spatially changing acceptance angle $\Delta\rho(\alpha, \varepsilon)$ was realized by adjusting the spacing between sampling directions accordingly while keeping the weight matrix constant.

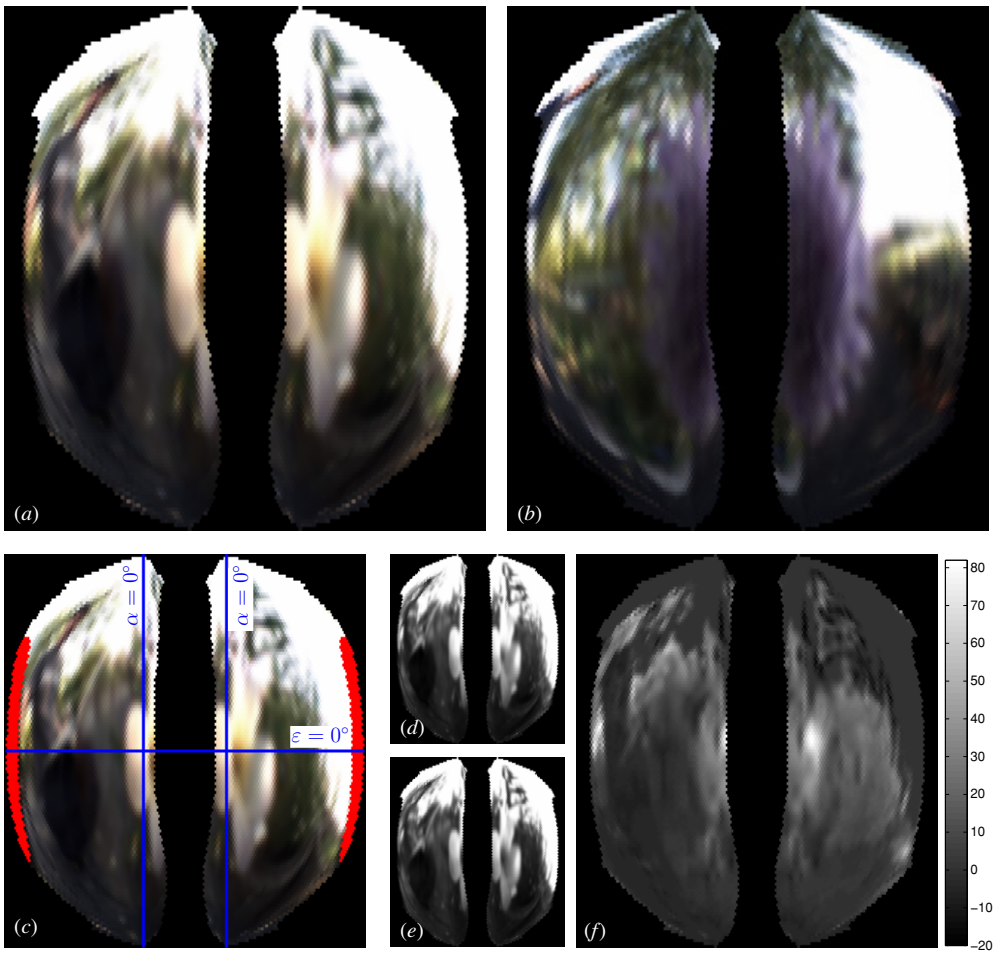

Figure 11. (*a*), (*b*) Ommatidial arrays as computed by the model for the two camera images shown in figures 5(*a*) and (*b*). Each ommatidium is displayed as a square of 2 × 2 pixels. In order to resemble the hexagonal arrangement of facets on the bee eye every second row is shifted by one pixel. Note that compared to figures 5(*c*) and (*d*), flowers are significantly enlarged due to higher resolution in the centre of the eyes. (*c*) Same as (*a*) but with ommatidia highlighted that have viewing directions outside the 280° FOV of our imaging system (these pixels are left black in (*a*), (*b*)). Lines mark the $\alpha = 0^\circ$ direction for each eye and the $\varepsilon = 0^\circ$ direction. (*d*), (*e*) The green and blue channel of the image in (*a*) shown as grey value images. (*f*) Difference of the green and blue channel.

Since the combined image has already limited resolution, which we estimated to be roughly equal to $\Delta\rho_{\text{img}} \approx 1.5^\circ$, the effective FWHM of the Gaussian acceptance function that has to be applied to the combined image is reduced according to

$$\Delta\rho_{\text{eff}}(\alpha, \varepsilon) = \sqrt{\Delta\rho(\alpha, \varepsilon)^2 - \Delta\rho_{\text{img}}^2}. \qquad (9)$$

Examples of the ommatidial arrays that were created from the combined images using the viewing directions of our bee eye model and the elevation-dependent Gaussian acceptance function are shown in figures 11(*a*) and (*b*). In this illustration each ommatidium has the same square area of 2 × 2 pixels. All remapping was done using look-up tables and bilinear pixel interpolation. Values of ommatidia are arranged in a manner that resembles the hexagonal facets in a bee's eyes. To achieve this, every second row is shifted by one pixel, i.e. half the width used for displaying an ommatidium. When comparing figures 11(*a*) and (*b*) with figures 5(*c*) and (*d*), the non-uniform sampling of the visual world by the eyes of a bee is clearly visible. Because vertical interommatidial angles decrease towards the equator of the eyes, elevation ranges closer to $\varepsilon = 0^\circ$ have higher resolution and thus occupy larger space in the *y*-direction than those closer to $\varepsilon = \pm 90^\circ$. This effect is even stronger on the bees' eyes since the diameter of ommatidia decreases with the distance from the centre of the eye. Please note that figure 11 is not an exact illustration of the arrangement of the ommatidia on a real bee's eye because (1) diameters of ommatidia increase with the absolute value of elevation on the real eye; (2) Seidl [1] identified regions in the eye with approximately constant interommatidial angles and reported the range of the angles in each region[7]. For calculating viewing directions, interommatidial angles have to be added up and even small deviations will accumulate. Thus, although local interommatidial angles are in the range measured by Seidl, it is likely that the model produces slightly different viewing directions than in the real eye; (3) the exact spatial arrangement, i.e. the 3D positions of ommatidia, was not reported in the literature and therefore not considered in the model (see also discussion). Ommatidia are rather arranged according to elevation (*y*-direction) and azimuth (*x*-direction),

[7] Seidl used three ranges for the horizontal interommatidial angle and five ranges for the vertical interommatidial angle.

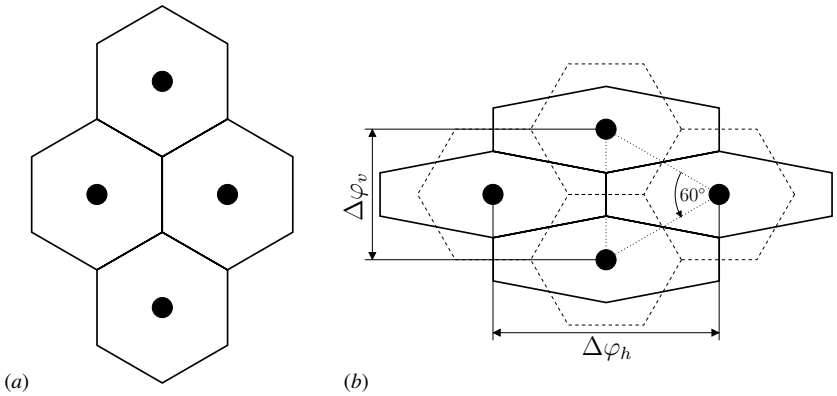

Figure 12. Illustration of how a difference might arise between the (approximately) hexagonal ommatidial lattice on the eye as seen, e.g., through a microscope (*a*) and the array of viewing directions (*b*). When looking at viewing directions, the original ommatidial lattice seems to be squashed in the vertical direction so that the array of viewing directions appears to be hexagonal as well (see the dashed hexagons) but oriented perpendicular to the ommatidial lattice. If viewing directions are evenly distributed locally, as depicted by the dotted equilateral triangle, then $\Delta\varphi_h$ has to be equal to $2\cos(\frac{1}{2}60^\circ)\,\Delta\varphi_v = \sqrt{3}\,\Delta\varphi_v$. In our model this is approximately true for the frontal and central regions of the eye, see figures 7 and 8.

see figure 11(*c*). Elevation is limited to −90° and to +90°, while in the dorsal and ventral rim of the real eye a few ommatidia view the contralateral side. Furthermore, rows of facets are not perfectly aligned in the real eye, and significant distortions of the ommatidial lattice exist at the border of the eye [22].

Figures 11(*d*) and (*e*) also show the green and blue channels separately which can be used as a first approximation to the responses of the green and blue photoreceptors of the bee. In this example, the region close to the centre of the flower that appears yellow to the human eye is also visible in the difference between the green and blue channel, figure 11(*f*). Colour contrast is used by honeybees for flower recognition and discrimination [26], and possibly for navigation as well.

5. Discussion and outlook

We have described a model of the compound eye of honeybees that describes viewing directions and angular sensitivities of ommatidia in agreement with measured interommatidial angles and acceptance angles. Moreover, we presented a small imaging system that covers almost the full FOV of bees using a single camera, enabling us to image a scene according to the spatial resolution of honeybees.

We extended the model of Giger [2] to the full FOV including the binocular overlap. The model determines viewing directions of ommatidia based on measured interommatidial angles [1]. As already mentioned, due to the summation of these angles when calculating viewing directions, small deviations from the viewing directions on the real eye are likely, in particular since Seidl [1] reports only the ranges of interommatidial angles within different areas on the eye. Also, in some parts of the eye our model produces non-hexagonally arranged viewing directions, see figures 7 and 9, and we do not know whether this is also the case in the real eye.

While viewing directions are most important for reconstructing the visual input, the exact positions of ommatidia might become relevant when viewing very close objects in particular in regions with binocular overlap. However due to the low resolution and the small stereo base, binocular depth perception, if it exists at all in honeybees, is certainly limited to very close objects. Having an overlapping zone might also serve other purposes that are not related to binocular depth perception like simplifying image processing. For example, it may be useful to have, during forward flight, the focus of expansion in both eyes without having to rely on information from the contralateral eye. Besides, the viewing part of a scene independently with two eyes improves the signal to noise ratio if the signals are pooled, which could be useful for low light levels.

As a further refinement, our model assumes that the acceptance angle is a function of the local interommatidial angles. As has been noticed by van Hateren and Backhaus [25], acceptance angles can be larger as expected from the diffraction limit and can not be inferred from the diameter of the lenses[8]. Thus, further measurements are necessary to determine if and how the acceptance angle changes with position. Also, the model produces circular angular sensitivity functions. While the vertical and horizontal acceptance angle have been repeatedly measured to be very similar in the frontal field of view [23, 24], we do not know whether this is true for the remaining part of the eye. Indeed for the specialized dorsal rim area, Labhart [24] reported slightly different acceptance angles when stimuli where moved lateral to medial compared to when moving anterior to posterior: $3.4^\circ \pm 0.4^\circ$ versus $2.8^\circ \pm 0.5^\circ$ and $5.7^\circ \pm 0.8^\circ$ versus $5.1^\circ \pm 0.8^\circ$. Non-circular receptive fields can be easily integrated into the model: as long as the sensitivity function is still Gaussian adjusting the spacing between sampling points will suffice to account for this. In order to improve the model in a way that it produces

[8] One might speculate that the function of a larger lens in regions of smaller interommatidial angles and possibly smaller acceptance angles is not primarily to reduce the diffraction limit but to improve light collection.

the ommatidial arrangement and exact mapping of the real eye, one would have to measure the location in addition to the viewing direction and acceptance angle of ommatidia. The shape of the real eye resembles part of an elongated ellipsoid and, as has been discussed in [25] for a frontal eye region, the pattern of viewing directions is usually different from the pattern of the ommatidia on the eye (see figure 12).

Despite the discussed limitations of our model of the spatial resolution of the honeybees compound eyes, we are confident that it is useful for many purposes, e.g. for the simulation of bee-like agents in virtual environments and, in combination with the presented imaging system, for testing bee-inspired visual navigation strategies on mobile robots. To reach a complete model of visual sensing in honeybees, colour vision, in particular in the near UV, and polarization vision needs to be included [24, 27]. Both topics will also be relevant when incorporating the second type of bee-eyes, the ocelli. Bees have three ocelli, one median and two lateral ones [22, 28], each equipped with a single lens that are involved in flight stabilization and related tasks [29, 30].

So far we have just considered the optical properties of the visual system of honeybees. For implementation of a bee-like control on a flying platform in the real world or a simulated agent acting in a virtual environment, photoreceptor dynamics and subsequent neuronal processing will have to be added as well [31–33]. The dynamics of photoreceptors like local gain control [31] cannot be achieved using standard camera sensors. While high dynamic range imaging may allow us to simulate photoreceptor dynamics after image capture [33], mimicking the high temporal resolution of visual processing in insects is challenging with respect to image acquisition as well as for the subsequent processing of images.

Acknowledgments

We thank the mechanical workshop, in particular Harald Wagner, of the DLR Robotics and Mechatronics Institute for machining the acrylic glass body and Risto Kõiva at Bielefeld University for 3D printing the plastic parts. This project was supported by the Deutsche Forschungsgemeinschaft (DFG).

Appendix. Rules for computing the viewing directions of ommatidia

We first describe the general scheme for computing the viewing directions and specify the parameters values in the subsequent paragraphs. For each of the four zones Z^z, $z = 1, 2, 3, 4$, defined by ranges in azimuth and elevation elevation angle, i.e.

$$Z^1: \quad 0^\circ \leqslant \alpha \leqslant 270^\circ, \qquad 0^\circ \leqslant \varepsilon \leqslant 90^\circ, \tag{A.1}$$

$$Z^2: \quad 0^\circ \leqslant \alpha \leqslant 270^\circ, \qquad -90^\circ \leqslant \varepsilon \leqslant 0^\circ, \tag{A.2}$$

$$Z^3: \quad -90^\circ \leqslant \alpha \leqslant 0^\circ, \qquad -90^\circ \leqslant \varepsilon \leqslant 0^\circ, \tag{A.3}$$

$$Z^4: \quad -90^\circ \leqslant \alpha \leqslant 0^\circ, \qquad 0^\circ \leqslant \varepsilon \leqslant 90^\circ, \tag{A.4}$$

a one dimensional array of elevation angles ε_i^k and a two-dimensional array of azimuth angles α_{ij}^k are created according to the following rules:

$$\begin{aligned}
&j = 0\\
&\varepsilon = 0^\circ\\
&\text{while} \quad |\varepsilon| \leqslant 90^\circ\\
&\qquad \varepsilon_j^z = \varepsilon\\
&\qquad i = 0\\
&\qquad \alpha = \begin{cases} 0^\circ, & j \text{ even} \\ \Delta\alpha\left(\xi_{\alpha^z}\Delta\varphi_h^{\text{mid}}/2, \varepsilon\right), & j \text{ odd} \end{cases}\\
&\qquad \text{while} \quad |\alpha| \leqslant |\alpha_{\max}^z(\varepsilon)|\\
&\qquad\qquad \alpha_{ij}^z = \alpha\\
&\qquad\qquad \Delta\varphi_h = \phi_h^z(\alpha, \varepsilon)\\
&\qquad\qquad \alpha = \alpha + \Delta\alpha(\Delta\varphi_h, \varepsilon)\\
&\qquad\qquad i = i + 1\\
&\qquad \text{end}\\
&\qquad \Delta\varphi_v = \Delta\varphi_v^{\min} + \left(\Delta\varphi_v^{\max} - \Delta\varphi_v^{\min}\right)\frac{|\varepsilon|}{90^\circ}\\
&\qquad \varepsilon = \varepsilon + \xi_\varepsilon^z\Delta\varphi_v/2\\
&\qquad j = j + 1\\
&\text{end}
\end{aligned} \tag{A.5}$$

The function

$$\Delta\alpha(\Delta\varphi_h, \varepsilon) = 2\arcsin\left(\frac{\sin(\Delta\varphi_h/2)}{\cos\varepsilon}\right) \tag{A.6}$$

transforms the horizontal interommatidial angle $\Delta\varphi_h$ that is given as an angle on a great circle, to increments of the azimuth angle [1, 2]. $\xi_\alpha^z = 1$ for the range $0^\circ \leqslant \alpha \leqslant 270^\circ$ (i.e. for Z^1 and Z^2), and $\xi_\alpha^z = -1$ for $-90^\circ \leqslant \alpha \leqslant 0^\circ$ (i.e. for Z^3 and Z^4); $\xi_\varepsilon^z = 1$ for the range $0^\circ \leqslant \varepsilon \leqslant 90^\circ$ (i.e. for Z^1 and Z^4) and $\xi_\varepsilon^z = -1$ for $-90^\circ \leqslant \varepsilon \leqslant 0^\circ$ (i.e. for Z^2 and Z^3). $\phi_h^z(\alpha, \varepsilon)$ defining the horizontal interommatidial angle and $\alpha_{\max}^z(\varepsilon)$ defining the maximum azimuth angle for each zone are given in the following paragraphs.

Horizontal interommatidial angle $\Delta\phi_h(\alpha, \varepsilon)$ for each zone. For Z^1 and Z^2 we used

$$\Delta\phi_h^{1/2}(\alpha, \varepsilon) = \begin{cases}
\Delta\varphi_h^{\text{mid}} + \frac{\alpha}{45^\circ}\left(\Delta\varphi_h^{\min} - \Delta\varphi_h^{\text{mid}}\right), \\
\quad 0^\circ \leqslant \alpha \leqslant 45^\circ \\
\Delta\varphi_h^{\min} + \frac{\alpha-45^\circ}{45^\circ}\left(\Delta\varphi_h^{\text{mid}} - \Delta\varphi_h^{\min}\right), \\
\quad 45^\circ < \alpha \leqslant 90^\circ \\
\Delta\varphi_h^{\text{mid}} + \frac{\alpha-90^\circ}{60^\circ}\left(\Delta\varphi_h^{\max} - \Delta\varphi_h^{\text{mid}}\right), \\
\quad 90^\circ < \alpha \leqslant 150^\circ, |\varepsilon| \leqslant 50^\circ \\
\Delta\varphi_h^{\text{mid}} + \frac{\alpha-90^\circ}{60^\circ}\left(\Delta\varphi_h^{\max} - \Delta\varphi_h^{\text{mid}}\right)\frac{90^\circ-|\varepsilon|}{40^\circ}, \\
\quad 90^\circ < \alpha \leqslant 150^\circ, |\varepsilon| > 50^\circ \\
\Delta\varphi_h^{\max}, \\
\quad 150^\circ < \alpha \leqslant 180^\circ, |\varepsilon| \leqslant 50^\circ \\
\Delta\varphi_h^{\text{mid}} + \left(\Delta\varphi_h^{\max} - \Delta\varphi_h^{\text{mid}}\right)\frac{90^\circ-|\varepsilon|}{40^\circ}, \\
\quad 150^\circ < \alpha \leqslant 180^\circ, |\varepsilon| > 50^\circ \\
\Delta\varphi_h^{\max}, \\
\quad 180^\circ < \alpha \leqslant 270^\circ;
\end{cases}$$

Table A1. Measured elevation angles and azimuth angles defining the border of the visible FOV for Z^1 and Z^2, i.e. in $0^\circ \leqslant \alpha \leqslant 270^\circ$. The continuous function $\alpha^{1/2}_{\max}(\varepsilon)$ is estimated from these values by means of cubic interpolation.

ε	-74.5°	-69.7°	-60.2°	-50.2°	-40.2°	-30.3°	-20.3°	-10.2°	0.0°
$\alpha_{\max}$	270.0°	191.9°	176.8°	174.6°	173.4°	166.8°	160.5°	158.5°	156.7°
ε	10.2°	20.2°	30.1°	39.9°	49.4°	58.9°	67.8°	69.0°	
$\alpha_{\max}$	158.5°	163.4°	174.3°	189.0°	202.4°	215.8°	244.7°	270.0°	

Table A2. Measured elevation angles and azimuth angles defining the border of the visible FOV for Z^3 and Z^4, i.e. in $-90^\circ \leqslant \alpha \leqslant 0^\circ$. The continuous function $\alpha^{3/4}_{\max}(\varepsilon)$ is estimated from these values by means of cubic interpolation.

ε	-74.5°	-67.8°	-58.1°	-48.5°	-38.9°	-29.4°	-19.8°	-9.9°	0.0°
$\alpha_{\max}$	-90.0°	-63.5°	-52.5°	-44.1°	-36.1°	-26.8°	-20.6°	-14.6°	-14.5°
ε	9.9°	19.8°	29.6°	39.4°	49.2°	58.9°	68.1°	69.0°	
$\alpha_{\max}$	-14.4°	-15.5°	-21.2°	-25.5°	-31.6°	-42.0°	-70.7°	-90.0°	

for Z^3,

$$\Delta\phi_h^3(\alpha,\varepsilon) = \begin{cases} \Delta\varphi_h^{\mathrm{mid}} + \frac{|\alpha|-45^\circ}{45^\circ}\left(\Delta\varphi_h^{\max} - \Delta\varphi_h^{\mathrm{mid}}\right)\frac{90^\circ-|\varepsilon|}{40^\circ}, \\ \quad -90^\circ \leqslant \alpha \leqslant -45^\circ, \varepsilon \leqslant -50^\circ \\ \Delta\varphi_h^{\mathrm{mid}}, \\ \quad -45^\circ \leqslant \alpha \leqslant 0^\circ, \quad \varepsilon \leqslant -50^\circ \\ \Delta\varphi_h^{\mathrm{mid}} + \frac{|\alpha|}{45^\circ}\left(\Delta\varphi_h^{\max} - \Delta\varphi_h^{\mathrm{mid}}\right)\frac{50^\circ-|\varepsilon|}{50^\circ}, \\ \quad -45^\circ < \alpha \leqslant 0^\circ, \quad -50^\circ < \varepsilon \leqslant 0^\circ; \end{cases}$$

and for Z^4,

$$\Delta\phi_h^4(\alpha,\varepsilon) = \begin{cases} \Delta\varphi_h^{\max} + \left(\Delta\varphi_h^{\max} - \Delta\varphi_h^{\mathrm{mid}}\right)\frac{90^\circ-|\varepsilon|}{40^\circ}, \\ \quad -90^\circ \leqslant \alpha \leqslant -45^\circ, \quad \varepsilon \geqslant 50^\circ \\ \Delta\varphi_h^{\mathrm{mid}} + \frac{|\alpha|}{45^\circ}(\Delta\varphi_h^{\max} - \Delta\varphi_h^{\mathrm{mid}}), \\ \quad -45^\circ < \alpha \leqslant 0^\circ, \quad 0^\circ < \varepsilon \leqslant 50^\circ \\ \Delta\varphi_h^{\mathrm{mid}} + \frac{|\alpha|}{45^\circ}\left(\Delta\varphi_h^{\max} - \Delta\varphi_h^{\mathrm{mid}}\right)\frac{90^\circ-\varepsilon}{40^\circ}, \\ \quad -45^\circ \leqslant \alpha \leqslant 0^\circ, \quad \varepsilon \geqslant 50^\circ. \end{cases}$$

The rules listed above depend on just five parameters defining the range of interommatidial angles:

$$\Delta\varphi_v^{\min} = 1.5^\circ, \qquad \Delta\varphi_v^{\max} = 4.5^\circ,$$
$$\Delta\varphi_h^{\min} = 2.4^\circ, \qquad \Delta\varphi_h^{\mathrm{mid}} = 3.7^\circ, \qquad \Delta\varphi_h^{\max} = 4.6^\circ.$$

These values are chosen so that they fall in the ranges reported by Seidl and give a realistic total number of ommatidia per eye. $\Delta\varphi_v^{\max}$ and $\Delta\varphi_h^{\mathrm{mid}}$ values deviate slightly from the corresponding values used in Giger's BEOS model [2]. These deviations are due to the fact that Seidl [1] did not report exact numbers but only ranges for the measured interommatidial angles (three ranges for the horizontal angle and five for the vertical interommatidial angles).

Maximum azimuth angle $\alpha^z_{\max}(\varepsilon)$ for each zone. For computing the maximum azimuth angle $\alpha^z_{\max}(\varepsilon)$ that defines the border of the visible FOV for the left eye, we used a piecewise cubic interpolation between the points measured by Seidl [1]. Tables A1 and A2 list the azimuth and elevation angles of these points calculated from the angles on great circles reported in [1].

References

[1] Seidl R 1982 Die Sehfelder und Ommatidien-Divergenzwinkel von Arbeiterin, Königin und Drohn der Honigbiene (*Apis mellifica*) *PhD Thesis* Technische Hochschule Darmstadt

[2] Giger A D 1996 Honeybee vision: analysis of pattern orientation *PhD Thesis* Australian National University

[3] Srinivasan M V, Zhang S, Altwein M and Tautz J 2000 Honeybee navigation: nature and calibration of the 'odometer' *Science* **287** 851–3

[4] Collett T S and Rees J A 1997 View-based navigation in hymenoptera: multiple strategies of landmark guidance in the approach to a feeder *J. Comp. Physiol.* A **181** 47–58

[5] Collett T 1996 Insect navigation en route to the goal: multiple strategies for the use of landmarks *J. Exp. Biol.* **199** 227–35

[6] Cartwright B A and Collett T S 1983 Landmark learning in bees *J. Comp. Physiol.* A **151** 521–43

[7] Benosman R and Kang S B (ed) 2001 *Panoramic Vision* (Berlin: Springer) ISBN: 978-0-387-95111-9

[8] Chahl J S and Srinivasan M V 1997 Reflective surfaces for panoramic imaging *Appl. Opt.* **36** 8275–85

[9] Baker S and Nayar S K 1999 A theory of single-viewpoint catadioptric image formation *Int. J. Comput. Vis.* **35** 175–96

[10] Hicks R A and Bajcsy R 2001 Reflective surfaces as computational sensors *Image Vis. Comput.* **19** 773–7

[11] Nagahara H, Yoshida K and Yachida M 2007 An omnidirectional vision sensor with single view and constant resolution *ICCV 2007: Int. Conf. on Computer Vision* pp 1–8 doi:10.1109/ICCV.2007.4409101

[12] Kweon G, Hwang-bo S, Kim G, Yang S and Lee Y 2006 Wide angle catadioptric lens with a rectilinear projection scheme *Appl. Opt.* **45** 8659–73

[13] Stürzl W and Srinivasan M V 2010 Omnidirectional imaging system with constant elevational gain and single viewpoint *OMNIVIS: 10th Workshop on Omnidirectional Vision, Camera Networks and Non-classical Cameras*

[14] Stürzl W, Soccol D, Zeil J, Boeddeker N and Srinivasan M V 2008 A rugged, obstruction-free, mirror-lens combination for panoramic imaging *Appl. Opt.* **47** 6070–8

[15] Land M F and Nilsson D-E 2002 *Animal Eyes* (Oxford: Oxford University Press) ISBN-10: 0198509685, ISBN-13: 978-0198509684

[16] Chiao C-C, Wu W-Y, Chen S-H and Yang E-C 2009 Visualization of the spatial and spectral signals of orb-weaving spiders, nephila pilipes, through the eyes of a honeybee *J. Exp. Biol.* **212** 2269–78

[17] Brückner A, Duparre J, Wippermann F, Dannberg P and Bräuer A 2009 Microoptical artificial compound eyes *Flying Insects and Robots* ed D Floreano, J-C Zufferey,

M V Srinivasan and C Ellington (Berlin: Springer) chapter 10, pp 127–42 (doi:10.1007/978-3-540-89393-6_10)
[18] Jeong K-H, Kim J and Lee L P 2006 Biologically inspired artificial compound eyes *Science* **312** 557–61
[19] Scaramuzza D, Martinelli A and Siegwart R 2006 A toolbox for easily calibrating omnidirectional cameras *IROS 2006: Int. Conf. on Intelligent Robots and Systems* pp 5695–5701 available at http://hal.inria.fr/inria-00359941/en/
[20] Faugeras O 1993 *Three-Dimensional Computer Vision—A Geometric Viewpoint* (Cambridge, MA: MIT Press) chapter 5 ISBN-10: 0-262-06158-9, ISBN-13: 978-0-262-06158-2
[21] Land M 1997 Visual acuity in insects *Annu. Rev. Entomol.* **42** 147–77
[22] Seidl R and Kaiser W 1981 Visual field size, binocular domain and the ommatidial array of the compound eyes in worker honey bees *J. Comp. Physiol.* A **143** 17–26
[23] Laughlin S B and Horridge G A 1971 Angular sensitivity of the retinula cells of dark adapted worker bee *Z. Vergl. Physiol.* **74** 329–39
[24] Labhart T 1980 Specialized photoreceptors at the dorsal rim of the honey-bee's compound eye: polarizational and angular sensitivity *J. Comp. Physiol.* A **141** 19–30
[25] van Hateren J H and Backhaus W Spatial sampling in the bee's eye *Technical Report* University of Groningen (http://hlab.phys.rug.nl/)
[26] Hempel de Ibarra N, Giurfa M and Vorobyev M 2002 Discrimination of coloured patters by honeybees *J. Comp. Physiol.* A **188** 503–12
[27] Chittka L 1992 The colour hexagon: a chromaticity diagram based on photoreceptor excitations as a generalized representation of colour opponency *J. Comp. Physiol.* A **170** 533–43
[28] Toh Y and Kuwabara M 1974 Fine structure of the dorsal ocellus of the worker honeybee *J. Morphol.* **143** 285–305
[29] Kastberger G 1990 The ocelli control the flight course in honeybees *Physiol. Entomol.* **15** 337–46
[30] Kastberger G and Schuhmann K 1993 Ocellar occlusion effect on the flight behavior of homing honeybees *J. Insect Physiol.* **39** 589–600
[31] van Hateren J H and Snippe H P 2001 Information theoretical evaluation of parametric models of gain control in blowfly photoreceptor cells *Vis. Res.* **41** 1851–65
[32] Lindemann J P, Kern R, van Hateren J H, Ritter H and Egelhaaf M 2005 On the computations analyzing natural optic flow: quantitative model analysis of the blowfly motion vision pathway *J. Neurosci.* **25** 6435–48
[33] Brinkworth R S A and O'Carroll D C 2009 Robust models for optic flow coding in natural scenes inspired by insect biology *PLoS Comput. Biol.* **5** e1000555